

More Bang For Your Buck(et): Fast and Space-efficient Hardware-accelerated Coarse-granular Indexing on GPUs

Justus Henneberg Felix Schuhknecht
Johannes Gutenberg University Mainz, Germany
{henneberg,schuhknecht}@uni-mainz.de

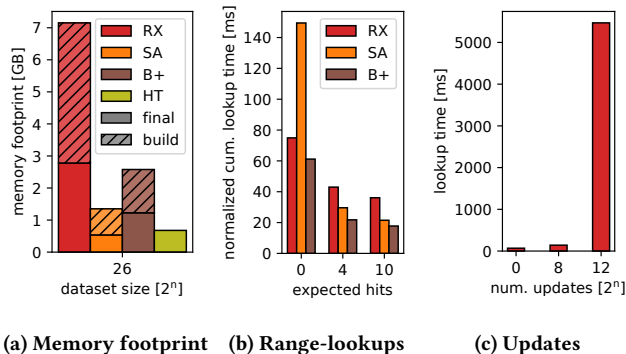
Rosina Kharal Trevor Brown
University of Waterloo, Canada
{rosina.kharal,trevor.brown}@uwaterloo.ca

ABSTRACT

In recent work, we have shown that NVIDIA’s raytracing cores on RTX video cards can be exploited to realize hardware-accelerated lookups for GPU-resident database indexes. On a high level, the concept materializes all keys as triangles in a 3D scene and indexes them. Lookups are performed by firing rays into the scene and utilizing the index structure to detect hits in a hardware-accelerated fashion. While this approach called **RTIndeX** (or short **RX**) is indeed promising, it currently suffers from three limitations: (1) significant memory overhead per key, (2) slow range-lookups, and (3) poor updateability. In this work, we show that all three problems can be tackled by a single design change: Generalizing **RX** to become a *coarse-granular* index **cgRX**. Instead of indexing individual keys, **cgRX** indexes buckets of keys which are post-filtered after retrieval. This drastically reduces the memory overhead, leads to the generation of a smaller and more efficient index structure, and enables fast range-lookups as well as updates. We will see that representing the buckets in the 3D space such that the lookup of a key is performed both correctly and efficiently requires the careful orchestration of firing rays in a specific sequence. Our experimental evaluation shows that **cgRX** offers the most bang for the buck(et) by providing a throughput in relation to the memory footprint that is 1.5–3× higher than for the comparable range-lookup supporting baselines. At the same time, **cgRX** improves the range-lookup performance over **RX** by up to 2× and offers practical updateability that is up to 5.5× faster than rebuilding from scratch.

1 INTRODUCTION

Utilizing hardware accelerators in creative ways to speed up database operations has become increasingly popular over the last years. A good example for this trend is our recent work **RTIndeX** [20], where we proposed **RX**, a hardware-accelerated index structure exploiting the raytracing cores present on modern NVIDIA video cards. The core idea is as follows: We represent every key in a dataset by a computer graphics primitive, such as a triangle, in a 3D scene. Then, we associate each primitive with the rowID of the key it represents. To perform a lookup of a specific key, we fire a ray through the area where the primitive representing the key is expected. If it collides with a primitive, the key was hit and the corresponding rowID is retrieved. To identify collisions between rays and primitives quickly, an index structure, namely a so-called bounding volume hierarchy (BVH), is constructed on all primitives. The key advantage is that on modern NVIDIA GPUs, both the BVH traversal as well as the ray-intersection tests in the leaf nodes are hardware-accelerated by dedicated raytracing cores, speeding up the lookup process without the need of manually hand-crafting a parallel GPU-resident index structure.

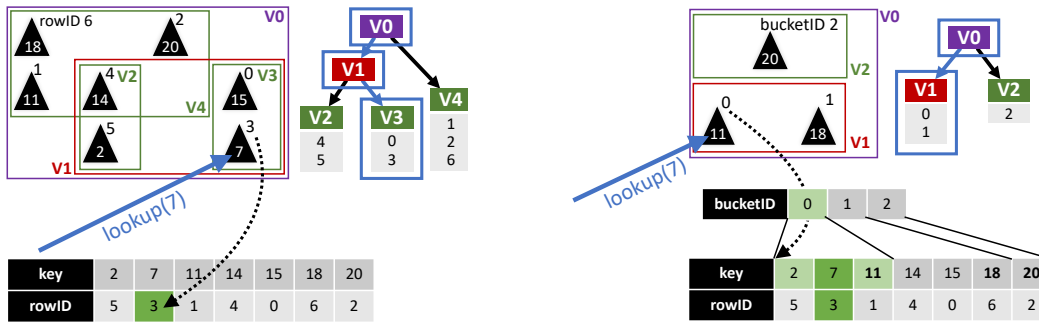


(a) Memory footprint (b) Range-lookups (c) Updates
Figure 1: Limitations of **RX**: Memory overhead, range-lookups, and lookup performance after updates [20].

While in [20], we showed that **RX** is largely competitive and in certain cases superior to traditional software-based index structures on GPUs [6, 8, 22], the approach also currently faces a set of unpleasant limitations. First of all, the memory overhead per key of **RX** is high since a single 64-bit integer key must be represented by a triangle described by nine 32-bit floats. As a result, 78% of the key representation is actually overhead. In the left plot in Figure 1, which has been generated from the results of [20], we can see that the traditional index structures have a significantly smaller memory footprint, which is mainly due to having less overhead per key. As memory is scarce on GPUs, this can be a drastic limitation for many applications. Second, range-lookups are currently a weakness of **RX**. In the middle plot in Figure 1, we can see that for all tested range sizes, the **B+**-tree clearly beats **RX**. The reason for this is that a range lookup in **RX** is carried out by a potentially large number of BVH traversals and ray-intersection tests with candidate triangles. In contrast, a **B+**-tree simply performs a *single* tree traversal for the lower bound key and then sequentially scans the leaf level. Third, **RX** is very sensitive to updates. Interestingly, the problem is not the cost of performing the updates, but a severe drop in lookup performance *after* the updates have been applied. The right plot in Figure 1 shows this by performing a batch of lookups after applying a varying number of updates: The more updates have been applied, the more the lookup performance deteriorates, up to a slowdown of 78× over no updates. The reason for this is that the BVH update procedure only scales the existing bounding volumes to reflect the updates, heavily increasing the number of intersection tests that must be carried out during lookups.

1.1 Towards Coarse-granular Indexing

Interestingly, the aforementioned limitations can be addressed by making a single design change: Instead of creating a *fine-granular* index **RX**, which maps individual keys to individual rowIDs via



(a) Fine-granular indexing in RX [20].

(b) Coarse-granular indexing in cgRX [this work].

Figure 2: Side-by-side comparison of the high-level principle of the original RX (Figure 2a) and our new cgRX (Figure 2b) when performing a point-lookup of key 7. Note that the generated BVH is significantly smaller for cgRX than for RX.

3D primitives, we propose to generalize the concept to a *coarse-granular index* **cgRX**, which sorts the key set and indexes it at the granularity of *buckets*. As a consequence, a lookup for a key does not return an individual rowID, but a bucketID instead. The bucket associated with the bucketID then contains a set of key-rowID pairs, which we search for the key(s) of interest. By adjusting which and how many keys are represented by a single bucket (and therefore, a single primitive), we can balance the cost of traversing the BVH, the cost of searching the bucket, and the memory footprint.

Figure 2 visualizes the high-level differences between the original fine-granular **RX** and our proposed coarse-granular **cgRX** for a set of 7 key-rowID pairs and a bucket size of 3. In **RX** in Figure 2a, each key is represented by a single triangle, resulting in a total of 7 triangles. In contrast to that, in **cgRX** in Figure 2b, only the last key of each bucket is materialized as a triangle and serves as a so-called representative, resulting in a total of only 3 triangles. By this the memory overhead decreased from 78% for **RX** to 48% for **cgRX** and a bucket size of 3. As the number of triangles correlates with the size of the generated BVH structure, **cgRX** also constructs a significantly smaller BVH than **RX**. This positively impacts the lookup performance, shown by performing a lookup of key 7. However, as **cgRX** returns a bucketID instead of a rowID directly, we have to perform a post-filtering step in the bucket. As we will see, the key challenge of realizing this principle is the arrangement of triangles in the scene as well as firing the rays in a way such that each search for a key actually hits the triangle representing its bucket. Depending on the situation, a lookup can now involve multiple consecutive rays being fired to safely detect a hit or miss.

1.2 Contributions and Structure of the Paper

In this work, we make the following contributions: (1) After re-capping the original method **RX** in Section 2, we present **cgRX**, our new hardware-accelerated coarse-granular index for NVIDIA RTX GPUs in Section 3. **cgRX** supports 64-bit keys as well as point and range-lookups. We discuss the construction and lookup procedure of a **naive representation**, which speeds up the navigation through the 3D scene by introducing explicit marker triangles. (2) Based on that, we present an **optimized representation**, which avoids materializing explicit marker triangles altogether. Instead, we turn a subset of representatives into implicit markers. This is

done by (a) moving certain representatives and (b) introducing auxiliary representatives in the scene. The evaluation shows that the optimized representation improves both lookup performance and memory footprint for very sparse key sets. (3) We present an extension of **cgRX** to support efficient batch-wise **updates** in Section 4. Insertions and deletions are handled by organizing buckets as a list of physical nodes, which are attached (or detached) on demand. By this, updates to the BVH and hence the extreme deterioration of the lookup performance is avoided. (4) As **cgRX** provides a set of **configuration parameters**, we analyze their impact for a variety of key distributions in Section 5. Precisely, we analyze the impact of (a) the key mapping into 3D space, (b) the bucket search method and bucket representation, as well as (c) the bucket size. (5) Using the best configuration(s), we perform an extensive **experimental evaluation** against a set of state-of-the-art baselines in Section 6. The evaluation analyzes (a) the throughput to memory footprint ratio, (b) the range-lookup performance, (c) the impact of the hit rate, (d) the impact of lookup skew, and (e) the update performance. Finally, we discuss related work (Section 7).

2 BACKGROUND

We start by discussing the working principle of the original method **RX** [20]. **RX** implements a fine-granular index, i.e., a structure which maps individual keys to individual rowIDs. The core idea of **RX** is to delegate traditional indexing of a single database column to a highly-optimized hierarchical index structure for geometric intersection problems (a bounding volume hierarchy, *BVH*). This is done by associating each possible 64-bit key with a unique position in 3D space. For each key k occurring in the column, a small triangle is created at the corresponding position in a 3D scene. This triangle also indirectly maps to the rowID of k . When looking up a key, **RX** probes the associated position in 3D space using raytracing and retrieves the rowID if it discovers a triangle at this position. By delegating the tracing part to NVIDIA’s OptiX computing API [13, 30], **RX** benefits from hardware acceleration via dedicated raytracing cores with each lookup.

2.1 Construction of RX

The construction of the index happens in two steps: First, the input column has to be transformed into a 3D scene, and then, the aforementioned BVH can be built on top of the 3D scene. Commonly, in computer graphics, 3D scenes consist of many small triangles that approximate the surfaces of the objects in the scene. **RX** does the exact opposite: For each key k in the column, **RX** inserts a single isolated triangle into the scene. This is done by storing the position of the three corner points in a so-called *vertex buffer*.

The position of the triangle in the 3D scene is computed using a *key mapping*. In [20], we observed that this key mapping cannot be arbitrary, but is limited to 23 bits in each dimension to ensure correct floating-point arithmetic. **RX** consequently uses a mapping where the 23 least significant bits of k are treated as the x coordinate, the next 23 bits as the y coordinate, and the 18 most significant bits as the z coordinate, denoted as $k \mapsto (k_{22:0}, k_{45:23}, k_{63:46})$. Due to the coordinate bit restrictions, the dimensional extent of the scene is bounded by $x_{max} = y_{max} = 2^{23} - 1$ and $z_{max} = 2^{18} - 1$. Geometrically speaking, the key mapping arranges the triangles into *rows* and *planes*: If two triangles share their y and z coordinate, we will describe them as being in the same row, and if they only share their z coordinate, we will refer to them as being on the same plane. This concept is visualized in Figure 3.

To associate a triangle with its rowID, the triangle is stored in the vertex buffer at position *rowID*. This position is called the *primitive index*, and it can be queried later on. The buffer is then passed to `optixAccelBuild()` to build the BVH, which indexes the individual triangles of the scene. A BVH is a tree-based index structure whose leaves represent triangles. To construct a BVH, triangles are disjointly grouped into three-dimensional cuboids (bounding volumes). Then, in a bottom-up fashion, these bounding volumes are grouped into larger bounding volumes again and again until only a single bounding volume remains. Figure 2a depicts an example BVH for seven triangles in two dimensions.

2.2 Lookups in RX

NVIDIA’s OptiX is designed to quickly find intersections between triangles and rays via hardware acceleration. Therefore, **RX** maps each lookup operation to a corresponding ray-triangle intersection problem. A ray is defined by its point of origin o and a three-dimensional direction vector d . To perform a point lookup of key k , one first computes the 3D position p associated with k , and then selects the ray parameters o and d so that the ray passes through this position. If a triangle exists at position p , the ray will intersect this triangle and retrieve the associated rowID. To prevent a ray from extending beyond a single triangle and producing false positives, OptiX provides an option to limit a ray to a specified length. Similarly, a range lookup $[l, u]$ can be performed by firing one or multiple rays in parallel to the x -axis, starting at the position associated with the lower bound l . Again, the ray is limited to not extend beyond the upper bound u . This way, only the triangles that are located between the given bounds will be hit, and we eventually obtain all rowIDs that are relevant to the lookup. As is typical for GPU-resident indexes, **RX** implements batch lookups to improve GPU utilization, where each lookup is performed by a single thread.

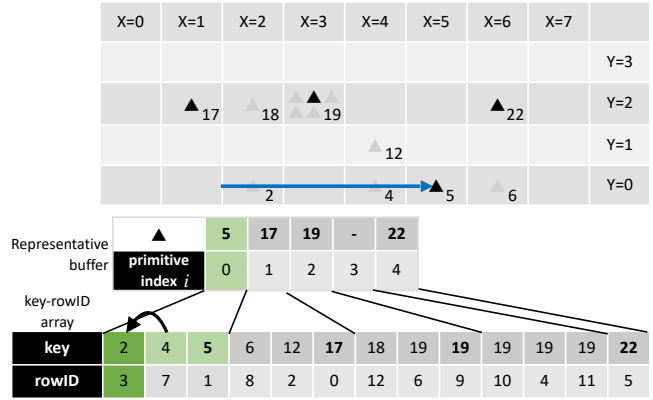


Figure 3: Example key set and associated triangle representation, followed by a lookup of key 2 which returns rowID 3. The representative ▲₅ of bucket 0 is located in the same row as the searched key 2. Row markers are hidden for simplicity.

3 COARSE-GRANULAR RX

Let us now discuss the specifics of our raytracing-based approach **cgRX**. Using a running example, we will present two different 3D scene representations, which **cgRX** can generate and query: A **naive representation** as well as an **optimized representation**, which requires fewer rays to be cast in certain situations while also having a lower memory footprint. To ease visualization, we will use a simpler key mapping in our examples, where the three last bits of the key determine the x coordinate, two bits determine the y coordinate, and the remainder determines the z coordinate, i.e., $k \mapsto (k_{2:0}, k_{3:2}, k_{63:4})$.

3.1 A Sparser Representation

With such a key mapping, each key can be uniquely represented as a triangle on an integer grid, just like in **RX**. This is exemplified in Figure 3, where we represent the keys as a set of triangles ▲ _{k} and ▲ _{k} . In **RX**, all of these triangles would be part of the scene, but in **cgRX**, we use a different strategy: Only the last triangle in each bucket is inserted as a *bucket representative*, shown as a black triangle ▲ _{k} . All remaining keys are *not* materialized in the scene but only stored in the key-rowID array. Nevertheless, we still visualize them as gray triangles ▲ _{k} . As a consequence of this design, the number of triangles we need to store in the vertex buffer is greatly reduced over **RX** which, in turn, reduces the size of the BVH.

At the same time, looking up a key k becomes more complex, since there is no guarantee that there will be a triangle at the position p associated with k . Instead, we need to search for the next bucket representative, which is always larger than or equal to k . So, the bucket representative either has to (1) be in the same row, but have a larger or equal x coordinate than p , or (2) be on the same plane, but have a larger y coordinate than p , or (3) be on a different plane and have a larger z coordinate than p .

Case (1) is visualized in Figure 3 for the lookup of key 2, where the triangle ▲₂ does not actually exist in the scene: To locate the bucket representative, we cast a **single ray** along the positive x -axis, starting our ray slightly left of ▲₂. The ray intersects ▲₅, which is the first triangle in the vertex buffer, and is therefore associated

Algorithm 1: Construction of the naive representation

```

Input: keys, bucketSize
Output: reps, markers, minRep, maxRep
1 minRep  $\leftarrow$  keys[bucketSize - 1], maxRep  $\leftarrow$  keys[len(keys) - 1]
2 multiLine  $\leftarrow$  minRep.yz  $\neq$  maxRep.yz
3 multiPlane  $\leftarrow$  minRep.z  $\neq$  maxRep.z
4 numBuckets  $\leftarrow$  ceil(len(keys) / bucketSize)
5 allocate reps[numBuckets]
6 allocate markers[(multiLine + multiPlane) · numBuckets]
7 for bucketID  $\leftarrow$  0 to numBuckets - 1 do in parallel
8   repIdx  $\leftarrow$  min((bucketID + 1) · bucketSize, len(keys)) - 1
9   rep  $\leftarrow$  keys[repIdx]
10  prevRep  $\leftarrow$  rep of previous bucket
11  if rep  $\neq$  prevRep then
12    | reps[bucketID] = mkTri(rep.x, rep.y, rep.z)
13  if multiLine and rep.yz  $\neq$  prevRep.yz then
14    | markers[bucketID] = mkTri(-1, rep.y, rep.z)
15  if multiPlane and rep.z  $\neq$  prevRep.z then
16    | markers[bucketID + numBuckets] = mkTri(-1, -1, rep.z)
17 return reps, markers, minRep, maxRep

```

If the lower bound l is larger than the largest key, we can safely report an empty result.

Markers. Whenever all representatives share the same plane or row, we skip the allocation of plane markers or even all markers. To retain correctness outside of this single plane or row, we supplement the tracing algorithm with additional checks (lines 1 and 2). The effect of this optimization is shown in Figures 3 and 4, which only contain row markers. Even so, in the worst-case, markers can inflate the size of the BVH by 3x, which is a problem that we will address in the optimized representation.

Algorithm 2: Point-lookup in the naive representation

```

Input: key, minRep, maxRep
Output: bucketID or MISS
1 if k < minRep then return 0
2 if k > maxRep then return MISS
3 sameRowHit  $\leftarrow$  xCast(key.x, key.y, key.z)
4 if sameRowHit then return sameRowHit.primitiveIndex
5 nextRowHit  $\leftarrow$  yCast(-1, key.y + 1, key.z)
6 if nextRowHit then
7   | sameRowHit  $\leftarrow$  xCast(0, nextRowHit.y, key.z)
8   | return sameRowHit.primitiveIndex
9 nextPlaneHit  $\leftarrow$  zCast(-1, -1, key.z + 1)
10 nextRowHit  $\leftarrow$  yCast(-1, 0, nextPlaneHit.z)
11 sameRowHit  $\leftarrow$  xCast(0, nextRowHit.y, nextPlaneHit.z)
12 return sameRowHit.primitiveIndex

```

3.3 Optimized Representation

Depending on the key distribution, it is possible that a single bucket spans multiple rows or even multiple planes. This is the reason why we have to potentially fire a whole sequence of rays to locate a representative. As firing more rays makes the lookup more expensive, in the following, we propose an optimized representation which

addresses this problem. At the same time, it potentially decreases the memory footprint. The high-level idea is based on two modifications which we are allowed to perform in the scene without harming correctness: (1) Let r be a representative and let k be the next key after r . Observe that we can replace r by another representative r' as long as $r < r' < k$, even if r' is not a key itself. In other words, we can *move* a representative as long as it does not collide with the next key. (2) Let r and r' be two adjacent representatives with $r < r'$. Then we are allowed to *insert* a new representative r'' between them so that $r < r'' < r'$. Since r'' falls into the bucket represented by r' , we need to associate r'' with the same bucketID as r' . Using these rules, we are able to ensure that each populated row ends with a representative in the last slot (at x_{max}), either by moving an existing representative there, or by inserting a new one.

Consequently, when starting a lookup in a populated row, we never have to fire more than a single ray as we will always find a representative there, therefore requiring less rays along the y -axis. Analogously, we can place a representative in the last slot of each populated plane to reduce the number of rays along the z -axis. At the same time, these newly inserted representatives can also serve as row/plane markers since they are always located at $x = x_{max}$ or $y = y_{max}$, as long as we change the respective offsets for yCast and zCast in Algorithm 2.

Algorithm 3: Construction of the optimized representation

```

Input: keys, bucketSize
Output: reps, minRep, maxRep
1 minRep  $\leftarrow$  keys[bucketSize - 1], maxRep  $\leftarrow$  keys[len(keys) - 1]
2 multiLine  $\leftarrow$  minRep.yz  $\neq$  maxRep.yz
3 multiPlane  $\leftarrow$  minRep.z  $\neq$  maxRep.z
4 numB  $\leftarrow$  ceil(len(keys) / bucketSize)
5 allocate reps[(1 + multiLine + multiPlane) · numB]
6 for bucketID  $\leftarrow$  0 to numB - 1 do in parallel
7   repIdx  $\leftarrow$  min((bucketID + 1) · bucketSize, len(keys)) - 1
8   rep  $\leftarrow$  keys[repIdx]
9   nextKey  $\leftarrow$  keys[repIdx + 1]
10  movable  $\leftarrow$  nextKey.yz  $\neq$  rep.yz
11  prevRep  $\leftarrow$  rep of previous bucket
12  nextRep  $\leftarrow$  rep of next bucket
13  needsRep  $\leftarrow$  rep  $\neq$  prevRep or (movable and rep.x  $\neq$   $x_{max}$ )
14  needsRowMark  $\leftarrow$  !movable and rep.yz  $\neq$  nextRep.yz
15  needsPlaneMark  $\leftarrow$  rep.y  $\neq$   $y_{max}$  and rep.z  $\neq$  nextRep.z
16  if needsRep then
17    | x  $\leftarrow$  if movable then  $x_{max}$  else rep.x
18    | doFlip  $\leftarrow$  movable and prevRep.yz  $\neq$  rep.yz
19    | reps[bucketID]  $\leftarrow$  mkTri(x, rep.y, rep.z, doFlip)
20  if multiLine and needsRowMark then
21    | reps[bucketID + numB]  $\leftarrow$  mkTri( $x_{max}$ , rep.y, rep.z)
22  if multiPlane and needsPlaneMark then
23    | reps[bucketID + 2 · numB]  $\leftarrow$  mkTri( $x_{max}$ ,  $y_{max}$ , rep.z)
24 return reps, minRep, maxRep

```

Construction. Algorithm 3 shows the pseudo-code for constructing this optimized representation. The code copies the single-row/single-plane optimization from the naive variant (lines 2 and 3),

but instead of allocating a separate marker buffer, it reserves additional space in the representative buffer (line 5), as the optimized variant does not differentiate between representatives and markers.

For each bucket, we need to check several conditions before placing the triangles. Following the observations listed above, a representative can be moved to the end of the row if the next key is not in the same row (line 10). This creates a special case for handling duplicate representatives: In the naive variant, we skipped insertion of all but the first representative to ensure that no two representatives exist at the same coordinates. In this variant, it is still possible to also insert the last representative of a duplicate group *if* it can be moved away from its initial position to the end of the row (line 13). If a representative is the last in its row and it cannot be moved, we have to explicitly insert a new representative at the end of the row (line 14). For bucket b , this triangle is placed in slot $b + \text{numBuckets}$ of the vertex buffer. Similarly, the bucket with the last representative on a plane generates an additional plane marker at $x = x_{\max}$, $y = y_{\max}$ in slot $b + 2 \cdot \text{numBuckets}$. If this last representative happens to be located in the last row of a plane ($y = y_{\max}$), we can skip its generation, since it coincides with the row marker (line 15).

Before continuing with an example, we have to address an optimization called *triangle flipping* in line 18. It applies whenever a representative can be moved to the end of the row while also being the only representative in this row. In this case, any ray being fired in the corresponding row will *always* hit this representative. Therefore, we do not need to fire this ray at all. To inform the lookup procedure of this fact, we “flip” the triangle by inverting the order in which the corner points are stored in the buffer (the winding order) from clockwise to counter-clockwise. This way, any ray fired along the y -axis will recognize the hit as a *back-side hit* as opposed to a *front-side hit*, and can react accordingly.

Figure 6 shows the optimized representation for our example key set. In comparison to the naive representation in Figure 3, we can see three differences: One representative is newly inserted as a marker (\blacktriangle_7) while another representative is moved (\blacktriangle_{23} replaces the representative \blacktriangle_{22} to its left) to serve as another marker. In exchange, no explicit markers are present anymore at $x = -1$.

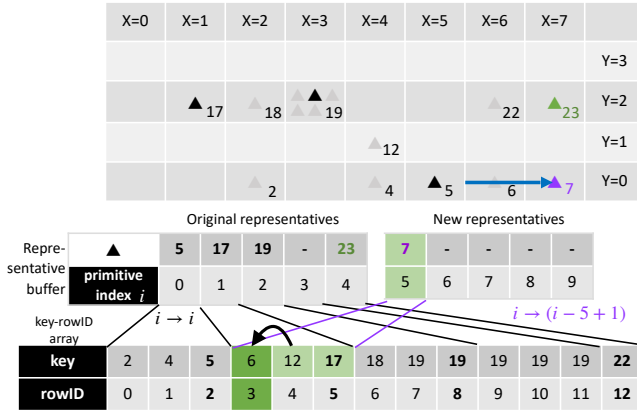


Figure 6: Visualization of the optimized representation.

Let us revisit the special cases from Algorithm 3: For the first bucket with bucketID 0, the representative \blacktriangle_5 must be materialized, as it is not a duplicate. However, we cannot materialize it at the end of the row, as its next key \blacktriangle_6 is located in the same row. Still, as \blacktriangle_5 is the last representative of the row, it is responsible for creating a new representative \blacktriangle_7 which serves as the row marker. Key 19 in row $y = 2$ appears multiple times, but since none of its instances are the last key in the row, there is no difference in how the representatives are placed compared to the naive algorithm. Instead, we move representative \blacktriangle_{22} , which happens to be the last key in the row, to the end of the row, producing \blacktriangle_{23} . Finally, we do not insert any plane markers, since all keys reside on a single plane. If we had to generate a plane marker, it would be located in the very last slot of the plane at $x = 7$ and $y = 3$.

Lookups. As shown in the figure, a lookup of key 6 (hit) is now answered by firing a *single ray* (hitting \blacktriangle_7), instead of *three rays*. Note that the primitive index $i = 5$ of \blacktriangle_7 is greater than the number of buckets, since \blacktriangle_7 is a newly inserted representative that has been stored after all regular representatives in the vertex buffer. Consequently, the primitive index has to be re-mapped to the corresponding bucketID by means of

$$i \mapsto \begin{cases} i - 2 \cdot \text{numBuckets} + 1 & \text{if } i \geq 2 \cdot \text{numBuckets} \\ i - \text{numBuckets} + 1 & \text{if } i \geq \text{numBuckets} \\ i & \text{otherwise} \end{cases}$$

which is cheap and easy to compute on a GPU.

3.4 Bucket Search and Bucket Representation

To search an individual bucket, we implement two different methods: (a) Linear search, which scans the bucket left-to-right. (b) Upper-bound binary search, which looks for the leftmost element larger than or equal to the target key. A bucket search is executed by the same thread that performs the raytracing. We evaluate the performance of both methods in Section 5.3.

The performance of the bucket search also depends on the way the key-rowID array is physically materialized. We support both a column layout, which materializes all keys in one array, and all rowIDs in a separate array, as well as a row layout, which materializes pairs of keys and rowIDs in a single array. Since we must support both 32-bit and 64-bit keys, but only require 32-bit rowIDs (as indexing more than 2^{32} entries would likely exceed the available GPU memory), we implement two variants here: An aligned variant, where all rows start at multiples of 8 bytes, even if they require padding, and a packed variant, where 64-bit keys are represented as two 32-bit numbers to circumvent the 8-byte alignment restriction. We evaluate the performance implications of the physical layout in Section 5.3.

4 HANDLING UPDATES

The presentation thus far has focused on a sorted array-based representation, but inserting into a globally sorted array requires shifting keys and rebuilding the BVH. Both are prohibitively expensive. So, to facilitate efficient updates, we propose a *node-based* variant of this representation.

The high level idea is to implement each *bucket* as a *linked list* of *nodes*. Nodes have a fixed size N , a tuneable parameter that

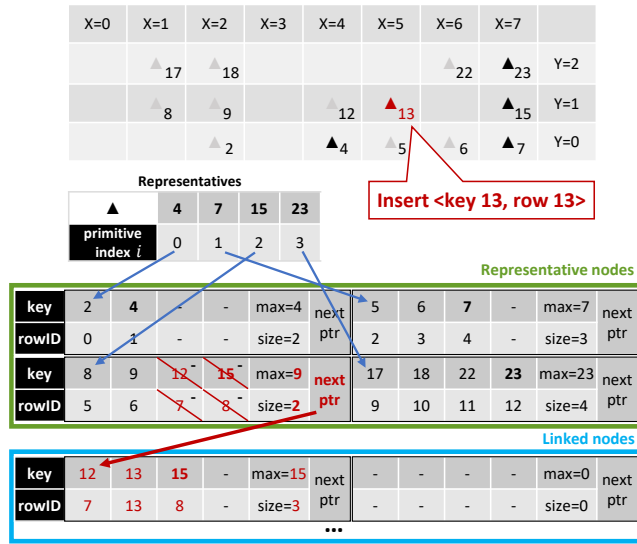


Figure 7: Node based representation for updates. Memory is partitioned into a green region where the data structure is initially built using contiguous nodes, and a blue region that is used to extend buckets when nodes are split.

we analyze in our experiments. Each node contains sorted *keys* and corresponding *rowIDs*, a *next* pointer, a *maxKey* and a current *size*. For each bucket, an initial *representative node* is created, and subsequent insertions into a bucket will cause this node to be *split*, resulting in the creation of a new node, and the movement of half of the keys into that new node. This is illustrated in Figure 7, which depicts a state some time after the initial construction of the index, after some subsequent insertions have happened, and a key-rowID pair (13, 13) is inserted. Nodes in a bucket can be split multiple times, and all nodes corresponding to a bucket are linked together using their *next* pointers, starting with the representative node. The nodes in a list each contain sorted keys, and are ordered in the list by their keys. This way, a point-lookup terminating at a representative node that has been split can simply follow *next* pointers to locate the relevant key, *without requiring the BVH or buckets to be updated*.

Rather than allocating each node individually, it is more efficient to allocate a large slab of memory, and manually partition it into nodes. Once this region has been entirely used, we enlarge it by allocating additional memory. We divide this large allocation into two subregions, one for representative nodes (*representative node region*), and the other for allocation of new nodes to be appended to linked lists (*linked node region*). Note that the next pointer of nodes can only be directed into the linked node region, as representative nodes are always the heads of their respective linked lists.

Initial construction. Given an array of key-rowID pairs for initial bulk loading, we first divide them into buckets of size $N/2$ (half the node size). We then create contiguous representative nodes for all buckets in the representative node region. These nodes are then filled in parallel until a specified fill state is reached using the key-rowID pairs of their respective buckets. Note that each representative triangle effectively points directly to the representative

node for its bucket. More precisely, since nodes are stored contiguously in the representative node region, the triangle’s primitive index can be multiplied by the size of a node, and added to the base address of the representative node region, to obtain the address of the representative node.

Point-lookups and range-lookups. The raytracing procedure to locate a bucket is unchanged, except for the calculation of the node address as explained above. Afterwards, we traverse the bucket chain starting at the representative node to find the last node where *maxKey* is greater than the key we are looking for. This node is then traversed using either linear search or binary search to obtain the rowID.

Insertion and deletion. Similar to lookups, keys to be inserted or deleted are collected in a batch that is then sent to the GPU in an array. The keys are then sorted. Any key that is both to be inserted and deleted in a batch can simply be eliminated from the batch. The actual insertion or deletion is handled by a CUDA kernel that dedicates one thread to each bucket in the current representation. The thread responsible for bucket *i* does two binary searches on the batch’s sorted keys to identify the sequence of keys it is responsible for, and traverses the nodes corresponding to bucket *i*, deleting and inserting these keys as appropriate. An advantage of allocating one thread per bucket is that there are no concurrency issues associated with updating a bucket (so, e.g., neither atomic read-modify-write instructions nor locks are needed).

Deletions are processed first, as by doing so, space may be created to facilitate insertions without splitting. For each key, the thread first locates the appropriate node in the list by comparing with the *maxKey* of each node. Then, it performs binary search to locate the appropriate index within the appropriate node. Deletion of a key results in keys to the right being shifted to the left. Insertion of a key results in shifting to the right. As explained above, insertion into a full node splits the node, changing its next pointer to point to a new node, and moving half of the keys into the new node. The new node receives the old node’s *maxKey*, and the old node’s largest key after the split becomes its new *maxKey*. If the new node is being inserted in the middle of a list, its next pointer is set to point to the following node.

Underutilized nodes. Empty (or nearly empty) nodes that result from updates can be dealt with in multiple ways. If such a node has a neighbour in its list, the two nodes can be *merged*. Note that since the first node in each list is part of the representative node region, in which nodes are contiguous, the first node in each list should not be merged into another node. Rather, the other node should be merged into the first node. If it is expected that nodes will infrequently be empty (or nearly empty), then periodically rebuilding the representation may be a simpler alternative.

Rebuilding. As insertions and deletions are performed, some buckets may become empty, or disproportionately large. A trivial solution is to periodically rebuild the data structure using the initial construction procedure. In future work, we plan to incorporate a reconstruction procedure which reuses and rearranges existing nodes whenever possible.

5 PARAMETER CONFIGURATION

In the following, we will experimentally analyze the impact of all configuration parameters of **cgRX**. Then, we will use the best configuration(s) in Section 6.

5.1 Setup & Key Distributions

We perform all of the following experiments on an NVIDIA RTX 4090 GPU with 24 GB of VRAM and 128 raytracing cores. This GPU implements the most recent Ada Lovelace architecture and is the fastest consumer RTX GPU currently available. The CPU is an AMD ThreadRipper 3990X.

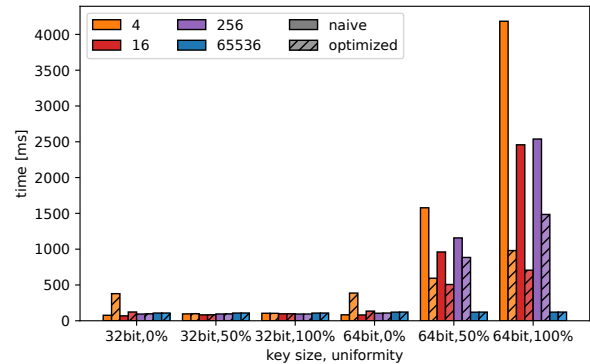
Unless specified otherwise, we generate a key set of 2^{26} keys consisting of 32-bit or 64-bit unsigned integers. The first part of the key set consists of all keys from 0 to $d - 1$ to reflect a dense key arrangement, and the second part is picked uniformly and randomly from the remaining value range to reflect a sparse key arrangement. We then shuffle the key sequence, and the final position in the shuffled sequence determines a key’s rowID. In the experiments, we vary the percentage of keys that are picked uniformly from 0% to 100%, which we simply refer to as the *uniformity* of the key set. Lookups are drawn randomly from the key set (unless specified otherwise) and we always perform 2^{27} lookups at once. The rowIDs obtained through the lookup are aggregated per-lookup, and then written to a separate result buffer to test for correctness.

Note that in all following experiments, we only measure the time it takes to obtain the aggregated rowIDs, and we never actually access any base table, as this would only yield constant cost for all indexes. This is different from [20], which always included the cost of accessing the base table.

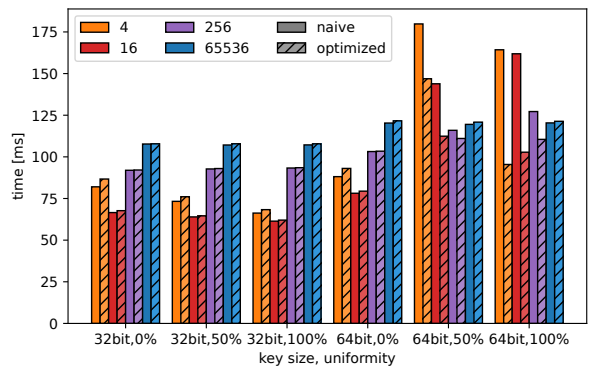
5.2 3D Representation and Key Mapping

First, we want to compare the naive and the optimized representation of **cgRX** in terms of point-lookup performance to see whether one variant performs consistently better than the other one. Therefore, Figure 8a shows for both representations the accumulated point-lookup time under the four bucket sizes 4, 16, 256, and 65,536 as well as the default key mapping used in [20], namely $k \mapsto (k_{22:0}, k_{45:23}, k_{63:46})$. We evaluate a key uniformity of 0%, 50%, and 100% and both 32-bit and 64-bit keys. Before going into the actual comparison, the results reveal an unexpected effect: If keys are picked from the 64-bit range and have a high uniformity (50% and 100%), the performance of both variants deteriorates heavily into the order of seconds. While a slowdown for these sparser key distributions is to be expected since on average more rays per lookup must be traced, this alone does not explain such a severe performance degradation.

Our hypothesis is that for these distributions, the proprietary BVH construction algorithm integrated in OptiX cannot choose a reasonable bounding volume layout due to the data being largely uniform. This renders the first (x -axis) ray, which is fired as part of every lookup, highly expensive. In Figure 9a, we conceptually visualize such a disadvantageous bounding volume clustering in two dimensions. In the example, the x -axis ray has to perform costly intersection tests with an unnecessarily large number of triangles since it also has to check for intersections in neighboring rows. Ideally, the bounding volumes would primarily extend along the x -axis,



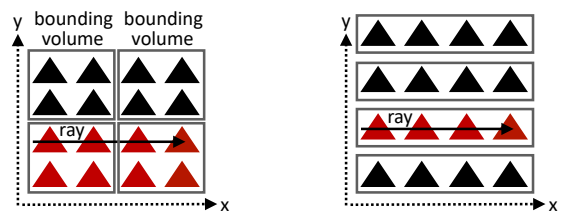
(a) Default key mapping in [20]: $k \mapsto (k_{22:0}, k_{45:23}, k_{63:46})$



(b) Scaled key mapping: $k \mapsto (k_{22:0}, 2^{15} \cdot k_{45:23}, 2^{25} \cdot k_{63:46})$

Figure 8: Impact of key mapping on the naive and optimized representation under different key distributions.

such that only the triangles in the current row have to be checked for intersection. To incentivize such a grouping, we simply adjust the key mapping slightly: We multiply both the y -coordinate $k_{45:23}$ and the z -coordinate $k_{63:46}$ with a large, carefully chosen constant. This effectively increases the space between triangles along these axes and guides the construction algorithm to prefer grouping along the x -axis, as visualized in Figure 9b, which is favorable for **cgRX**.



(a) No scaling: If the construction algorithm groups along the y -axis, horizontal rays have to perform intersection tests with a large number of triangles.

(b) Scaling the y -axis: This guides the construction algorithm to group along the x -axis, which results in less intersection tests for horizontal rays.

Figure 9: Visualization of the impact of scaling on the BVH structure (shown for two dimensions). All red triangles must be tested for intersection.

To validate this strategy, we scaled both the y -axis and the z -axis using a variety of constants and looked for an impact on the lookup time. Consistently, we achieved the best results for the mapping $k \mapsto (k_{22:0}, 2^{15} \cdot k_{45:23}, 2^{25} \cdot k_{63:46})$, which scales both axes so significantly that the construction algorithm reliably groups along the x -axis. Figure 8b shows the results using this mapping. As we can see, the point-lookup performance of both the naive and optimized representation has improved significantly. *Consequently, in all upcoming experiments, we will use the scaled mapping.*

Coming back to the initial comparison of the naive and optimized representations, we can observe in Figure 8b that for 32-bit key sets, both variants perform equally well. From a geometric perspective, 32-bit keys are always arranged on a single plane. The amount of rays for lookups is therefore limited to three, with most lookups requiring only one ray. Therefore, the optimized scene representation does not yield significant improvements. However, for the 64-bit key sets with a high uniformity (and hence, high sparsity), optimizing the representatives significantly shortens the lookup procedure and improves the performance. Inspecting the number of individually fired rays for each variant reveals that for smaller buckets, the optimized representation avoids firing the second x -axis ray in most cases, because the previous y -axis ray hit a flipped representative. Apart from the performance, our experimental results also confirm that the optimized representation reduces the memory footprint over the naive representation for sparse key sets: For example, for 64-bit keys and a bucket size of 4, the optimized representation saves 16% and 28% memory over the naive one for a uniformity of 50% and 100%, respectively. *Hence, we will continue using only the optimized representation in the following.*

5.3 Comparing Bucket Search and Layout

After identifying the best scene representation, we evaluate how to materialize the buckets in memory and how to search within them. For four different bucket sizes, we measure the accumulated point-lookup performance for linear search and binary search. For both search strategies, we evaluate all three layouts, resulting in six tested configurations per bucket size. Also, we focus on 64-bit keys and fix the uniformity to 100%.

bucket size	binary search			linear search		
	column layout	row layout		column layout	row layout	
		aligned	packed		aligned	packed
4	108.4	97.5	95.5	108.4	97.5	100.3
16	113.4	109.5	102.8	118.2	135.2	119.2
256	120.6	121.2	110.5	551.8	1113.6	824.2
65,536	132.0	133.2	121.3	-	-	-

Table 1: Impact of bucket config. for a uniformity of 100%.

Table 1 shows the results. Focusing on the search method first, we can see that binary search performs better or at least equally well when compared to linear search in all cases. This even holds for very small buckets, where we expected an advantage for linear search due to lesser code complexity. When using large buckets, linear search becomes infeasible. *Consequently, we use only binary search in all following experiments.* In terms of bucket representation, the row layouts generally perform better than the column layout. Among the row layouts, the packed layout is clearly superior over

the aligned layout for larger buckets, since the smaller memory footprint results in smaller data transfers. *Hence, we only consider the packed row layout from here on.*

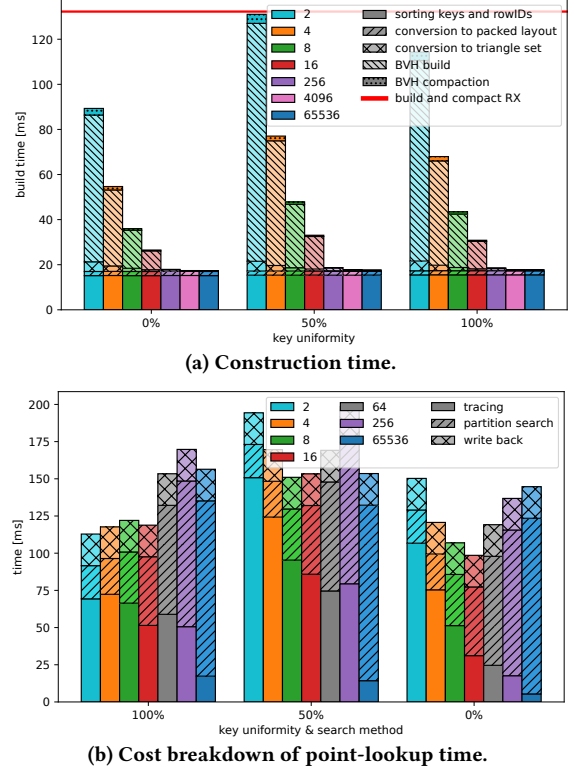


Figure 10: Impact of the bucket size.

5.4 Finding the Bucket Size

So far, we used four exemplary bucket sizes for the evaluation. In the following, we will inspect the impact of different bucket sizes in more detail. Intuitively, the larger the bucket size the smaller the memory footprint and the faster the construction, because a smaller BVH is created. However, with an increase in bucket size, the cost for searching the buckets increases as well. In Figure 10, we analyze this trade-off for 64-bit key sets with a varying uniformity and bucket sizes ranging from 2 to 65,536 in logarithmic steps.

Figure 10a shows the construction time of **cgRX**, which we break down into (1) sorting the keys and rowIDs, (2) converting of the key-rowID set into packed row layout, (3) converting the key set into a triangle set, (4) building the BVH, and (5) compacting the BVH. Additionally, we show the total construction time of the original **RX** as a baseline. We can observe that as expected, the total construction time decreases with an increase in bucket size: While for a bucket size of 2, the construction takes between 98ms and 134ms, it drops to less than 20ms for a bucket size of 256 and larger. The breakdown reveals that a majority of cost is caused by the BVH construction (3), which halves with a doubling of the bucket size. We can also observe that the construction time of **cgRX** is in nearly all cases below the construction time of **RX**, even for very small buckets. Note that the construction time also correlates to the memory footprint: While

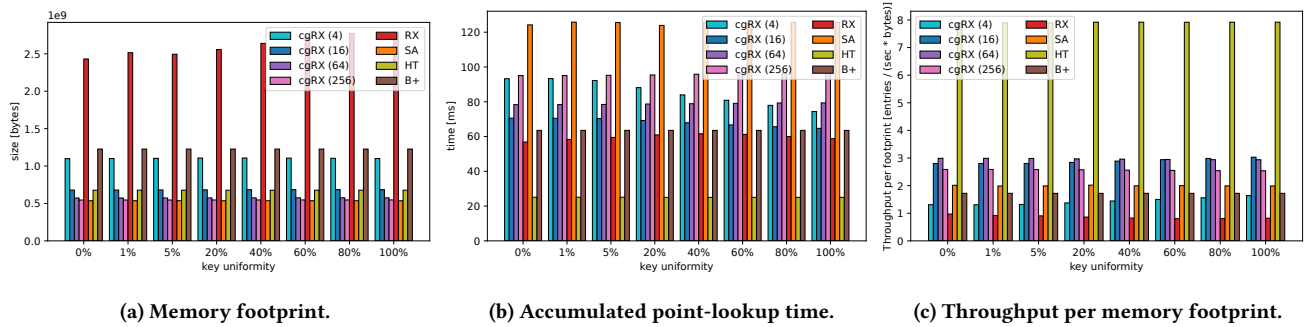


Figure 11: Comparison of memory footprint and point-lookup performance for key range $[0, 2^{32} - 1]$.

for a bucket size of 2, the memory footprint is between 1.77GiB and 2.12GiB, it decreases to only 0.75GiB for a bucket size of 65,536. Therein, the BVH only requires 11.5MB of memory, while the key-rowID array consumes the rest.

In Figure 10b, we perform a breakdown of the point-lookup time while varying the bucket size, where we split the time into (1) firing all rays, (2) all bucket searches, and (3) writing the results. Note that to measure the individual phases, we adjusted the lookup procedure slightly: Instead of performing all three phases in one pipeline, we first retrieve all bucketIDs using OptiX and then search the corresponding buckets in a separate GPU program. This causes some overhead, but is the only way to accurately measure the phases. The results show that (1) improves with an increase in bucket size, while (2) becomes more expensive and (3) remains constant. For each key distribution, we also observe a specific sweet spot, which moves depending on the key distribution.

Size recommendation. We conducted extensive experiments to measure the impact of bucket size on performance over a variety of key distributions and index sizes, and entertained the idea of producing a cost model to predict the correct bucket size, given an index size and distribution estimate. Unfortunately, the impact of bucket size is quite complex, so we instead settle for a single recommendation, **16**, that results in middle-of-the-road performance over a wide variety of measured workloads. Still, in the following, we report the measurements for other bucket sizes as well.

6 EXPERIMENTAL EVALUATION

In the following, we evaluate how assorted configurations of **cgRX** perform against a set of competitive baselines. We use the same baselines as in [20]: **HT**: A GPU-resident open addressing hash table [22, 23], which performs cooperative probing. The target load factor is set to the recommended 80%. **B+**: A GPU-resident B+ tree [9, 18], which uses CUB’s DeviceRadixSort [12] for sorting and 16-thread tree traversal. It only supports 32-bit keys. **SA**: A GPU-resident Sorted Array [20] also using CUB’s DeviceRadixSort [12] for sorting and binary search for lookups. Further, we compare against the original fine-granular **RX**.

6.1 Memory Footprint and Point-lookups

One of our central motivations for **cgRX** was to reduce the memory footprint of the original **RX** approach *while* providing good performance. To find out whether **cgRX** achieves this goal, Figure 11a

shows the permanent memory footprint of all methods on 32-bit key sets with varying uniformity. For **cgRX**, we evaluate the bucket sizes 4, 16, 64, and 256. As expected, **RX** has by far the highest footprint between 2.2GiB (0% uniformity) and 2.6GiB (100% uniformity). In comparison, even for a small bucket size of 4, **cgRX** shows a significantly lower memory footprint of only around 1.0GiB, which is already less than the footprint of **B+** at around 1.1GiB. For a bucket size of 16, **cgRX** is on par with **HT**, whereas for a bucket size of 64, **cgRX** even approaches the space-optimal **SA**. We want to emphasize that the shown bucket sizes are not chosen artificially large to optimize the memory footprint, but rather lie within the range of the performance sweet spots observed in Figure 10b. Thus, even when setting the bucket size to optimize for performance and *not* for space consumption, **cgRX** achieves an impressive memory footprint.

In Figure 11b, we shift the focus to the point-lookup performance of all methods. **HT** performs the fastest lookups at around 25ms and **SA** performs the worst at around 125ms, with **RX** and **B+** positioning themselves between these two at 60ms and 65ms, respectively. For all key distributions, **cgRX** achieves its best performance for a bucket size of 16, where it almost reaches the performance of **B+**, especially under a key set with a high uniformity.

To bring both memory footprint and point-lookup performance into perspective, Figure 11c aggregates the information of Figure 11a and Figure 11b. Precisely, we show the throughput of each method as entries per second, which is additionally divided by the memory footprint in bytes. By this, we essentially visualize how each method pays for its throughput capabilities with its memory footprint, i.e., by building auxiliary lookup structures. Again, **HT** wins in this regard, as it is both fast and space-efficient. However, when focusing on indexes that also support range lookups, **cgRX** clearly outperforms all remaining indexes for the bucket sizes of 16, 64, and 256. In particular, in its best configuration for the respective key set, its throughput per memory footprint is 3× higher than for **RX**, 1.75× higher than for **B+**, and 1.5× higher than for **SA**. Not that we observed a similar trend for 64-bit keys: For bucket sizes 16 and 64, **cgRX** outperforms all other indexes supporting range lookups, showing a 1.8× and 1.54× higher throughput per memory footprint than **RX** and **SA**, respectively. This means that overall, **cgRX** provides the best “bang for the buck” of all general-purpose GPU-resident indexes, a property which is especially important in the presence of scarce GPU memory.

6.2 Range Lookups

Next, we inspect the range-lookup performance, where we mimic the experimental setup used for range lookups in [20]. This means we use a 32-bit key set with a uniformity of 0% (dense) and vary the number of expected hits per range-lookup from 1, which resembles a point-lookup, to 1024. We report the normalized cumulative lookup time, which is the total time of all range lookups divided by the total number of retrieved entries. Note that **HT** does not support range lookups, and is therefore not included in this evaluation.

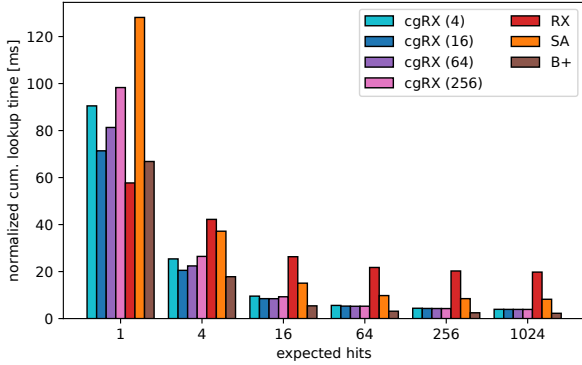


Figure 12: Range-lookups on a dense 23-bit key range.

Figure 12 shows the results. We can see that for all lookups which return more than one entry, **cgRX** outperforms **RX** and **SA** for all tested bucket sizes and remedies the poor range-lookup performance of the original **RX**. The reason for this is that **cgRX** must perform only one point-lookup per range-lookup, followed by a simple scan. In contrast, **RX** must detect all qualifying entries in the collision detection of its tracing procedure, which is prohibitively expensive. For a selectivity of 4 hits per range-lookup, the best configuration of **cgRX** using a bucket size of 16 is more than 2× and 1.8× faster than **RX** and **SA**, respectively, and only 1.15× times slower than **B+**. Investigation showed that the slight advantage of **B+** stems mainly from performing the final aggregation step using warp-reductions, while **cgRX** aggregates naively.

6.3 Varying the Hit Ratio

So far, all point-lookups resulted in hits. To see the impact of misses, in the following, we fire a certain amount of point lookups that do not hit an indexed key and report the accumulated point-lookup time. We additionally differentiate between misses that lie within the value range of the indexed data, and ones that lie outside of that range. The key set consists of 32-bit keys with uniformity 100%.

Figure 13 shows the results. We observe that while **RX** strongly benefits from misses, this is unfortunately not the case for **cgRX**. The reason for this is that **RX** is able to abort the BVH traversal as soon as it detects that a key is not covered by any bounding volume. This is not possible for **cgRX** which always finds a representative if the target key is within the value range. Consequently, the miss is detected rather late during the bucket search process. This means that **cgRX** should be primarily used in hit-only or hit-mostly lookup scenarios. The last two bars show the effect of out-of-range misses: Here, the search is trivial, and **cgRX** can finish quickly.

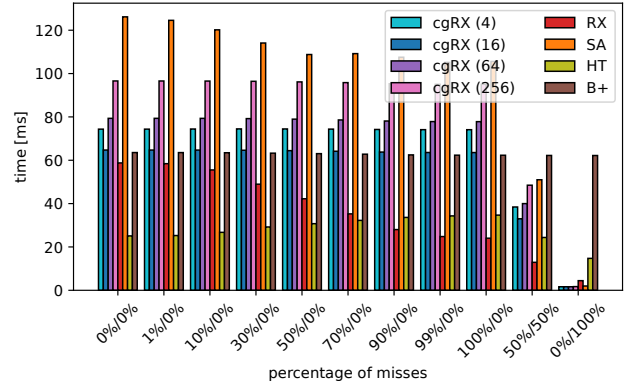


Figure 13: Varying the hit ratio.

6.4 Varying the Lookup Skew

In all previous experiments, we picked the lookup keys uniformly from the key range. In the following, we test the effect of skewed lookups, which follow a Zipf distribution. We include the uniform distribution seen so far by using a Zipf coefficient of 0.0, and evaluate different levels of skewness by varying the coefficient from 0.25 (low skew) to 5.0 (extreme skew). On the y-axis, we report the accumulated point-lookup time.

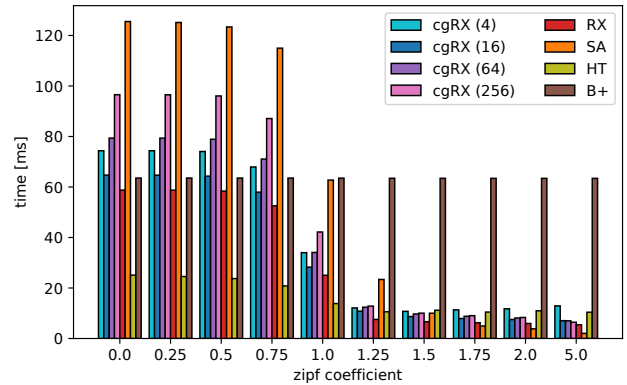


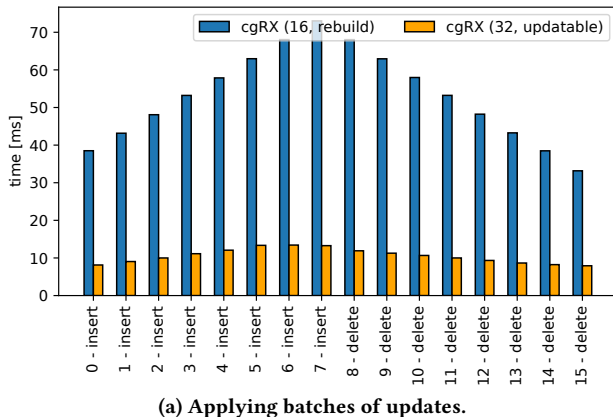
Figure 14: Varying the skew of lookups.

In Figure 14, we can observe that skew is generally beneficial from a performance perspective, as it increases the chance of cache hits and therefore reduces memory accesses. **B+** is an outlier here, where the lookup time is apparently unaffected by skew. NVIDIA’s kernel profiler shows that cache hits indeed increase dramatically with higher skew values for **B+**, but the execution is bottlenecked by the so-called address divergence unit, which handles block synchronization and divergent branches.

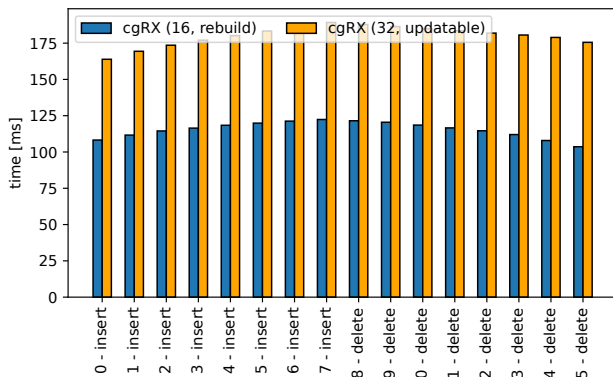
6.5 Updates

Finally, let us investigate how well our node-based update mechanism performs. We compare it against the alternative of rebuilding the entire structure from scratch for every batch of updates, which was the only practical way of applying updates in [20].

Initially, we bulk-load both variants with our usual 2^{26} 64-bit keys, following a uniformity of 100%. Then, we fire eight waves of equally-sized insertion batches, where each insertion batch is followed by a lookup batch of size 2^{27} . We configure these waves of insertions such that in total, the number of indexed entries is increased by $2.2\times$. Afterwards, we perform eight corresponding deletion waves, again interleaved with lookups. These deletion waves deflate the key set again to its original size. We configure our updateable method with a node size of 32, where only half of each node is filled initially. This leaves some headroom for inserts, but is obviously not sufficient to handle the $2.2\times$ inflation. The baseline method without update support uses a bucket size of 16, such that the total number of buckets is the same for both methods. Figure 15a shows the time to apply the individual update waves on both variants, while Figure 15b shows the time to perform the corresponding lookup batches after each update wave has been applied. We can see that our method reduces the cost of applying updates by up to $5.5\times$ in comparison to full rebuilds. Also, the cost of updating our updateable variant increases at a slower rate than the cost of fully rebuilding. For lookups, we can observe that the overhead of introducing linked lists of nodes to represent buckets is relatively small – and could potentially be further improved as currently, not all optimizations of the read-only variant are integrated (such as triangle flipping).



(a) Applying batches of updates.



(b) Performing point-lookups after updates have been applied.

Figure 15: Updating cgRX vs rebuilding it from scratch.

7 RELATED WORK

Apart from the original **RX** [20], there exists a line of work from other areas that exploits hardware-accelerated raytracing. These include point containment tests [25, 29, 34, 38], time-of-flight imaging [28, 33, 36], radius search [15, 41], graph rendering [39], and particle movement [10, 11, 35]. All these application share that they rely on some sort of intersection tests, which benefit from the RT-core provided hardware acceleration.

In terms of indexes, many data structures have been ported to become GPU-resident in recent years, which typically involves optimizing the memory layout and access pattern to fit to the underlying architecture. GPU-resident indexes include hash tables [2–4, 21, 23, 26, 40], from which we picked our baseline **HT**, but also bloom filters [14, 19, 23] and quotient filters [16] which are suitable for set-containment tests and trade memory footprint with false-positive accuracy. Further, radix trees [1] and comparison-based trees [5, 7, 9, 24] also exist for GPUs and additionally provide range-lookup support. While our evaluation includes a state-of-the-art comparison-based tree **B+**, unfortunately, no code of the radix tree is available. There also exist GPU-resident spatial indexes such as R-Trees [31, 37] or GPU permutation indexes [27]. While they would offer a great baseline for our comparisons since they construct bounding volumes, there is unfortunately currently also no code available for these indexes.

In terms of APIs, apart from OptiX [30], which we utilized in our implementation, DirectX [32] and Vulkan [17] also provide means to realize hardware-accelerated raytracing. The concept of **cgRX** could be realized using these APIs as well. Note that OptiX also supports other primitive types which could serve as a replacement for the triangle primitives in **cgRX**. These include spheres, which have a curved surface defined by a center point and a radius, as well as axis-aligned bounding boxes (AABBs), which resemble rectangular boxes. Since we have shown in [20] that both offer worse performance than triangles, since their intersection test is currently not hardware-accelerated, we did not consider them in this work.

8 CONCLUSION

We presented **cgRX**, a coarse-granular GPU-resident index which exploits hardware acceleration via RT-cores and overcomes the main limitations of its fine-granular predecessor **RX**, namely high memory footprint, poor range-lookup performance, and bad updateability. We have shown that **cgRX** provides the most bang for buck by offering a $1.5\text{--}3\times$ higher throughput in relation to the memory footprint than the tested state-of-the-art GPU-resident indexes that support both point of range-lookups. At the same time, **cgRX** provides competitive range-lookup and update performance.

REFERENCES

- [1] Md. Maksudul Alam, Srikanth B. Yoganath, and Kalyan S. Perumalla. 2016. Performance of Point and Range Queries for In-memory Databases Using Radix Trees on GPUs. In *18th IEEE International Conference on High Performance Computing and Communications; 14th IEEE International Conference on Smart City; 2nd IEEE International Conference on Data Science and Systems, HPCC/SmartCity/DSS 2016, Sydney, Australia, December 12-14, 2016*, Jinjun Chen and Laurence T. Yang (Eds.). IEEE Computer Society, 1493–1500. <https://doi.org/10.1109/HPCC-SmartCity-DSS.2016.0212>
- [2] Dan A. Alcantara, Andrei Sharf, Fatemeh Abbasnejad, Shubhabrata Sengupta, Michael Mitzenmacher, John D. Owens, and Nina Amenta. 2009. Real-time

- parallel hashing on the GPU. *ACM Trans. Graph.* 28, 5 (2009), 154. <https://doi.org/10.1145/1618452.1618500>
- [3] Dan A. Alcantara, Vasily Volkov, Shubhabrata Sengupta, Michael Mitzenmacher, John D. Owens, and Nina Amenta. 2012. Chapter 4 - Building an Efficient Hash Table on the GPU. In *GPU Computing Gems Jade Edition*, Wen mei W. Hwu (Ed.). Morgan Kaufmann, Boston, 39–53. <https://doi.org/10.1016/B978-0-12-385963-1.00004-6>
 - [4] Saman Ashkiani, Martin Farach-Colton, and John D. Owens. 2018. A Dynamic Hash Table for the GPU. In *2018 IEEE International Parallel and Distributed Processing Symposium, IPDPS 2018, Vancouver, BC, Canada, May 21-25, 2018*. IEEE Computer Society, 419–429. <https://doi.org/10.1109/IPDPS.2018.00052>
 - [5] Saman Ashkiani, Shengren Li, Martin Farach-Colton, Nina Amenta, and John D. Owens. 2018. GPU LSM: A Dynamic Dictionary Data Structure for the GPU. In *2018 IEEE International Parallel and Distributed Processing Symposium, IPDPS 2018, Vancouver, BC, Canada, May 21-25, 2018*. IEEE Computer Society, 430–440. <https://doi.org/10.1109/IPDPS.2018.00053>
 - [6] Muhammad A. Awad, Saman Ashkiani, Rob Johnson, Martin Farach-Colton, and John D. Owens. 2019. Engineering a high-performance GPU B-Tree. In *Proceedings of the 24th ACM SIGPLAN Symposium on Principles and Practice of Parallel Programming, PPoPP 2019, Washington, DC, USA, February 16-20, 2019*, Jeffrey K. Hollingsworth and Idit Keidar (Eds.). ACM, 145–157. <https://doi.org/10.1145/3293883.3295706>
 - [7] Muhammad A. Awad, Saman Ashkiani, Rob Johnson, Martin Farach-Colton, and John D. Owens. 2019. Engineering a high-performance GPU B-Tree. In *Proceedings of the 24th ACM SIGPLAN Symposium on Principles and Practice of Parallel Programming, PPoPP 2019, Washington, DC, USA, February 16-20, 2019*, Jeffrey K. Hollingsworth and Idit Keidar (Eds.). ACM, 145–157. <https://doi.org/10.1145/3293883.3295706>
 - [8] Muhammad A. Awad, Serban D. Porumbescu, and John D. Owens. 2022. A GPU Multiversion B-Tree. In *Proceedings of the International Conference on Parallel Architectures and Compilation Techniques, PACT 2022, Chicago, Illinois, October 8-12, 2022*, Andreas Klöckner and José Moreira (Eds.). ACM, 481–493. <https://doi.org/10.1145/3559009.3569681>
 - [9] Muhammad A. Awad, Serban D. Porumbescu, and John D. Owens. 2022. A GPU Multiversion B-Tree. In *Proceedings of the International Conference on Parallel Architectures and Compilation Techniques, PACT 2022, Chicago, Illinois, October 8-12, 2022*, Andreas Klöckner and José Moreira (Eds.). ACM, 481–493. <https://doi.org/10.1145/3559009.3569681>
 - [10] Pascal R. Bähr, Bruno Lang, Peer Ueberholz, Marton Ady, and Roberto Kersevan. 2022. Development of a hardware-accelerated simulation kernel for ultra-high vacuum with Nvidia RTX GPUs. *Int. J. High Perform. Comput. Appl.* 36, 2 (2022), 141–152. <https://doi.org/10.1177/10943420211056654>
 - [11] Blyth, Simon. 2020. Meeting the challenge of JUNO simulation with Opticks: GPU optical photon acceleration via NVIDIA OptiX. *EPJ Web Conf.* 245 (2020), 11003. <https://doi.org/10.1051/epjconf/202024511003>
 - [12] NVIDIA Corporation. 2022. CUB. <https://nvlabs.github.io/cub/> Accessed on February 27th, 2023.
 - [13] NVIDIA Corporation. 2023. NVIDIA OptiX. <https://developer.nvidia.com/rtx/ray-tracing/optix> Accessed: February 27, 2023.
 - [14] Lauro B. Costa, Samer Al-Kiswany, and Matei Ripeanu. 2009. GPU support for batch oriented workloads. In *28th International Performance Computing and Communications Conference, IPCCC 2009, 14-16 December 2009, Phoenix, Arizona, USA*. IEEE Computer Society, 231–238. <https://doi.org/10.1109/IPCCC.2009.5403809>
 - [15] I. Evangelou, G. Papaioannou, K. Vardis, and A. A. Vasilakis. 2021. Fast Radius Search Exploiting Ray Tracing Frameworks. *Journal of Computer Graphics Techniques (JCGT)* 10, 1 (5 February 2021), 25–48. <http://jcgt.org/published/0010/01/02/>
 - [16] Afton Geil, Martin Farach-Colton, and John D. Owens. 2018. Quotient Filters: Approximate Membership Queries on the GPU. In *2018 IEEE International Parallel and Distributed Processing Symposium, IPDPS 2018, Vancouver, BC, Canada, May 21-25, 2018*. IEEE Computer Society, 451–462. <https://doi.org/10.1109/IPDPS.2018.00055>
 - [17] Khronos Group. 2020. Ray Tracing in Vulkan. <https://www.khronos.org/blog/ray-tracing-in-vulkan> Accessed: February 27, 2023.
 - [18] Owens Research Group. 2021. MVGpuBTree: Multi-Value GPU B-Tree. <https://github.com/owensgroup/MVGpuBTree> Accessed: February 27, 2023.
 - [19] Masatoshi Hayashikawa, Koji Nakano, Yasuaki Ito, and Ryota Yasudo. 2019. Folded Bloom Filter for High Bandwidth Memory, with GPU Implementations. In *2019 Seventh International Symposium on Computing and Networking, CANDAR 2019, Nagasaki, Japan, November 25-28, 2019*. IEEE, 18–27. <https://doi.org/10.1109/CANDAR.2019.00011>
 - [20] Justus Henneberg and Felix Schuhknecht. 2023. RTIdx: Exploiting Hardware-Accelerated GPU Raytracing for Database Indexing. *Proc. VLDB Endow.* 16, 13 (2023), 4268–4281. <https://www.vldb.org/pvldb/vol16/p4268-schuhknecht.pdf>
 - [21] Daniel Jünger, Christian Hundt, and Bertil Schmidt. 2018. WarpDrive: Massively Parallel Hashing on Multi-GPU Nodes. In *2018 IEEE International Parallel and Distributed Processing Symposium, IPDPS 2018, Vancouver, BC, Canada, May 21-25, 2018*. IEEE Computer Society, 441–450. <https://doi.org/10.1109/IPDPS.2018.00054>
 - [22] Daniel Jünger, Robin Kobus, André Müller, Christian Hundt, Kai Xu, Weiguo Liu, and Bertil Schmidt. 2020. WarpCore: A Library for fast Hash Tables on GPUs. In *27th IEEE International Conference on High Performance Computing, Data, and Analytics, HiPC 2020, Pune, India, December 16-19, 2020*. IEEE, 11–20. <https://doi.org/10.1109/HIPC50609.2020.00015>
 - [23] Daniel Jünger, Robin Kobus, André Müller, Christian Hundt, Kai Xu, Weiguo Liu, and Bertil Schmidt. 2020. WarpCore: A Library for fast Hash Tables on GPUs. In *27th IEEE International Conference on High Performance Computing, Data, and Analytics, HiPC 2020, Pune, India, December 16-19, 2020*. IEEE, 11–20. <https://doi.org/10.1109/HIPC50609.2020.00015>
 - [24] Changkyu Kim, Jatin Chhugani, Nadathur Satish, Eric Sedlar, Anthony D. Nguyen, Tim Kaldewey, Victor W. Lee, Scott A. Brandt, and Pradeep Dubey. 2010. FAST: fast architecture sensitive tree search on modern CPUs and GPUs. In *Proceedings of the ACM SIGMOD International Conference on Management of Data, SIGMOD 2010, Indianapolis, Indiana, USA, June 6-10, 2010*, Ahmed K. Elmagarmid and Divyakant Agrawal (Eds.). ACM, 339–350. <https://doi.org/10.1145/1807167.1807206>
 - [25] Moritz Laass. 2021. Point in Polygon Tests Using Hardware Accelerated Ray Tracing. In *SIGSPATIAL '21: 29th International Conference on Advances in Geographic Information Systems, Virtual Event / Beijing, China, November 2-5, 2021*, Xiaofeng Meng, Fusheng Wang, Chang-Tien Lu, Yan Huang, Shashi Shekhar, and Xing Xie (Eds.). ACM, 666–667. <https://doi.org/10.1145/3474717.3486796>
 - [26] Yuchen Li, Qiwei Zhu, Zheng Lyu, Zhongdong Huang, and Jianling Sun. 2021. DyCuckoo: Dynamic Hash Tables on GPUs. In *37th IEEE International Conference on Data Engineering, ICDE 2021, Chania, Greece, April 19-22, 2021*. IEEE, 744–755. <https://doi.org/10.1109/ICDE51399.2021.00070>
 - [27] Mariela Lopresti, Fabiana Piccoli, and Nora Reyes. 2021. GPU Permutation Index: Good Trade-Off Between Efficiency and Results Quality. In *Computer Science - CACIC 2021 - 27th Argentine Congress, CACIC 2021, Salta, Argentina, October 4-8, 2021, Revised Selected Papers (Communications in Computer and Information Science, Vol. 1584)*, Patricia Pesado and Gustavo Gil (Eds.). Springer, 183–200. https://doi.org/10.1007/978-3-031-05903-2_13
 - [28] Mogamat Yaaseen Martin, Simon Lucas Winberg, Mohammed Yunus Abdul Gaffar, and David MacLeod. 2022. The Design and Implementation of a Ray-tracing Algorithm for Signal-level Pulsed Radar Simulation Using the NVIDIA® OptiX Engine. *J. Commun.* 17, 9 (2022), 761–768. <https://doi.org/10.12720/jcm.17.9.761-768>
 - [29] Nate Morrical, Ingo Wald, Will Usher, and Valerio Pascucci. 2022. Accelerating Unstructured Mesh Point Location With RT Cores. *IEEE Trans. Vis. Comput. Graph.* 28, 8 (2022), 2852–2866. <https://doi.org/10.1109/TVCG.2020.3042930>
 - [30] Steven G. Parker, James Bigler, Andreas Dietrich, Heiko Friedrich, Jared Hoberock, David P. Luebke, David K. McAllister, Morgan McGuire, R. Keith Morley, Austin Robinson, and Martin Stich. 2010. OptiX: a general purpose ray tracing engine. *ACM Trans. Graph.* 29, 4 (2010), 66:1–66:13. <https://doi.org/10.1145/1778765.1778803>
 - [31] Sushil K. Prasad, Michael McDermott, Xi He, and Satish Puri. 2015. GPU-based Parallel R-tree Construction and Querying. In *2015 IEEE International Parallel and Distributed Processing Symposium Workshop, IPDPS 2015, Hyderabad, India, May 25-29, 2015*. IEEE Computer Society, 618–627. <https://doi.org/10.1109/IPDPSW.2015.127>
 - [32] Microsoft DirectX Team. 2018. Announcing Microsoft DirectX Raytracing! <https://devblogs.microsoft.com/directx/announcing-microsoft-directx-raytracing/> Accessed: February 27, 2023.
 - [33] Peter Thoman, Markus Wippler, Robert Hranitzky, and Thomas Fahringer. 2020. RTX-RSim: Accelerated Vulkan Room Response Simulation for Time-of-Flight Imaging. In *Proceedings of the International Workshop on OpenCL (Munich, Germany) (IWOC '20)*. Association for Computing Machinery, New York, NY, USA, Article 17, 11 pages. <https://doi.org/10.1145/3388333.3388662>
 - [34] Ingo Wald, Will Usher, Nathan Morrical, Laura Lediaev, and Valerio Pascucci. 2019. RTX Beyond Ray Tracing: Exploring the Use of Hardware Ray Tracing Cores for Tet-Mesh Point Location. In *High-Performance Graphics 2019 - Short Papers, Strasbourg, France, July 8-10, 2019*, Markus Steinberger and Theresa Foley (Eds.). Eurographics Association, 7–13. <https://doi.org/10.2312/hpg.20191189>
 - [35] Bin Wang, Ingo Wald, Nate Morrical, Will Usher, Lin Mu, Karsten E. Thompson, and Richard Hughes. 2022. An GPU-accelerated particle tracking method for Eulerian-Lagrangian simulations using hardware ray tracing cores. *Comput. Phys. Commun.* 271 (2022), 108221. <https://doi.org/10.1016/j.cpc.2021.108221>
 - [36] Qiang Wang, Bo Peng, Ziyuan Cao, Xing Huang, and Jingfeng Jiang. 2020. A Real-time Ultrasound Simulator Using Monte-Carlo Path Tracing in Conjunction with Optix Engine. In *2020 IEEE International Conference on Systems, Man, and Cybernetics, SMC 2020, Toronto, ON, Canada, October 11-14, 2020*. IEEE, 3661–3666. <https://doi.org/10.1109/SMC42975.2020.9283057>
 - [37] Simin You, Jianting Zhang, and Le Gruenwald. 2013. Parallel spatial query processing on GPUs using R-trees. In *Proceedings of the 2nd ACM SIGSPATIAL International Workshop on Analytics for Big Geospatial Data, BigSpatial@SIGSPATIAL 2013, Nov 4th, 2013, Orlando, FL, USA*, Varun Chandola and Rangaj R. Vatsavai (Eds.). ACM, 23–31. <https://doi.org/10.1145/2534921.2534949>

- [38] Stefan Zellmann, Daniel Seifried, Nate Morriscal, Ingo Wald, Will Usher, Jamie A. P. Law-Smith, Stefanie Walch-Gassner, and André Hinkenjann. 2022. Point Containment Queries on Ray-Tracing Cores for AMR Flow Visualization. *Comput. Sci. Eng.* 24, 2 (2022), 40–51. <https://doi.org/10.1109/MCSE.2022.3153677>
- [39] Stefan Zellmann, Martin Weier, and Ingo Wald. 2020. Accelerating Force-Directed Graph Drawing with RT Cores. In *31st IEEE Visualization Conference, IEEE VIS 2020 - Short Papers, Virtual Event, USA, October 25-30, 2020*. IEEE, 96–100. <https://doi.org/10.1109/VIS47514.2020.00026>
- [40] Kai Zhang, Kaibo Wang, Yuan Yuan, Lei Guo, Rubao Lee, and Xiaodong Zhang. 2015. Mega-KV: A Case for GPUs to Maximize the Throughput of In-Memory Key-Value Stores. *Proc. VLDB Endow.* 8, 11 (2015), 1226–1237. <https://doi.org/10.14778/2809974.2809984>
- [41] Yuhao Zhu. 2022. RTNN: accelerating neighbor search using hardware ray tracing. In *PPoPP '22: 27th ACM SIGPLAN Symposium on Principles and Practice of Parallel Programming, Seoul, Republic of Korea, April 2 - 6, 2022*, Jaejin Lee, Kunal Agrawal, and Michael F. Spear (Eds.). ACM, 76–89. <https://doi.org/10.1145/3503221.3508409>